# Magnetic Order Unlocks Optical Access to Dark Excitons in CrSBr

Sophie Bork<sup>a</sup>, Richard Leven<sup>a</sup>, Vincent Wirsdörfer<sup>a</sup>, Alessandro Ferretti<sup>b</sup>, Rafael R. Rojas-Lopez<sup>a</sup>, Mattia Benini<sup>a</sup>, David Maximilian Janas<sup>a</sup>, Umut Parlak<sup>c</sup>, Alberto Brambilla<sup>b</sup>, Alexey V. Scherbakov<sup>a</sup>, Mirko Cinchetti<sup>a,\*</sup>

<sup>a</sup>Department of Physics, TU Dortmund University, Dortmund, Germany

<sup>b</sup>Dipartimento di Fisica, Politecnico di Milano, 20133 Milan, Italy

<sup>c</sup>Fachbereich Physik, Universität Konstanz, Konstanz, 78457 Germany

Corresponding author: \* mirko.cinchetti@tu-dortmund.de

#### **Abstract**

Hybrid quasiparticles that intertwine magnetic and electronic degrees of freedom underpin emerging strategies for manipulating and transducing quantum information in solids<sup>1</sup>. A key missing element has been the ability to optically access dark excitons—optically forbidden but functionally crucial states that shape energy flow, coherence, and spin dynamics in quantum materials<sup>2–4</sup>. Here we show that exciton—magnon coupling provides an optical gateway to dark excitons in the antiferromagnetic van der Waals semiconductor CrSBr. Broadband femtosecond reflectivity reveals a dark exciton at 1.46 eV that is entirely absent in static optical spectra but becomes visible through its coherent hybridization with a GHz magnon. High-photon-energy excitation further allows active control of the hybrid dispersion, enabling strong renormalization and selective enhancement of exciton—magnon interactions. These results establish a general mechanism by which magnetic order renders dark excitons optically addressable, opening a pathway toward engineered hybrid spin—exciton platforms for microwave-to-optical quantum transduction.

**Keywords:** Exciton-magnon coupling, van der Waals magnets, transient reflectivity, dark excitons, CrSBr semiconductor

#### Introduction

The interplay between magnetic order and electronic excitations in quantum materials offers a powerful platform for engineering new hybrid quasiparticles with functionalities unattainable in conventional semiconductors<sup>1,5,6</sup>. In van der Waals magnets<sup>6–9</sup>, reduced dimensionality and strong Coulomb interactions give rise to robust excitons<sup>10</sup> alongside long-range magnetic order, enabling excitons to couple directly to collective spin excitations<sup>1</sup>. Such exciton–magnon coupling provides a natural route toward optical manipulation of magnetic degrees of freedom and forms the basis for proposals ranging from exciton-mediated control of spin dynamics<sup>4,11</sup> to microwave-to-optical quantum transduction<sup>1</sup> —the coherent conversion of quantum information between microwave and optical domains. These hybrid spin–exciton platforms offer opportunities for quantum interconnects and optoelectronic devices, making magnetic van der Waals materials increasingly central to quantum technologies. Yet a key element of this landscape—the role of dark excitons, which dominate relaxation pathways but remain optically forbidden—has remained largely inaccessible.

Dark excitons play a central role in valleytronics<sup>2</sup>, exciton transport<sup>3</sup>, and coherence dynamics<sup>12</sup> in atomically thin semiconductors, but detecting them typically requires momentum-resolved probes or tailored selection rules, and their interaction with magnetic excitations has remained unexplored. Steady-state optical techniques struggle to reveal these states because they carry little or no oscillator strength<sup>13–15</sup>. Time-resolved ARPES can visualize momentum-indirect dark excitons<sup>16,17</sup>, but it provides limited insight into their coupling to spin order. Consequently, whether and how dark excitons participate in exciton–magnon hybridization is an open question with direct implications for the design of hybrid quantum interfaces.

CrSBr, a two-dimensional antiferromagnetic semiconductor with highly anisotropic electronic structure<sup>18–20</sup>, provides an ideal platform to address this question. It exhibits long-range antiferromagnetic order below 132 K<sup>21–24</sup> and a direct near-infrared band gap<sup>25</sup>. Its excitonic spectrum is dominated by strongly bound, polarization-selective resonances, with two primary bright excitons at 1.36 eV and 1.77 eV<sup>1,26–29</sup>. The antiferromagnetic order supports GHz-frequency magnons that modulate the optical response<sup>30,31</sup>. Bright excitons in CrSBr have been shown to couple coherently to magnons, giving rise to oscillatory optical signatures near 1.36 eV<sup>30</sup>. More recently, a dark exciton near 1.45 eV has been identified through resonant inelastic x-ray scattering<sup>32</sup>, indicating that the material hosts hidden excitonic degrees of freedom whose optical signatures remain elusive.

Here we show that magnetic order provides optical access to this dark exciton by enabling its coherent hybridization with a magnon mode. Using broadband femtosecond reflectivity that resolves the low-energy excitonic resonances of CrSBr (1.25–1.65 eV), we uncover a pronounced oscillatory response at 1.46 eV that is absent in static optical spectra. This response carries the hallmarks of a discrete excitonic resonance, including a characteristic  $\pi$ -phase flip in the time-domain modulation, and emerges only through its interaction with a coherent magnon. We further demonstrate that high-photon-energy excitation strongly renormalizes the magnon dispersion and enhances its coupling to excitonic states, enabling tunability of the hybrid mode.

These results establish a general mechanism by which magnetic order renders dark excitons optically addressable, expanding the toolbox for probing hidden quasiparticles in quantum materials and opening a pathway toward engineered exciton—magnon platforms for hybrid quantum technologies.

#### **Results and discussion**

**Figure 1a** illustrates the experimental configuration for the transient reflectivity measurements on bulk CrSBr crystals at 80 K, with an external magnetic field applied out of plane, parallel to the crystallographic c-axis. The pump and probe beams were incident at near-normal angles. The pump photon energy was tuned from near resonance with the excitonic transitions (near-resonant, NR; 1.72 eV) to a high-photon-energy, off-resonant regime (high-energy, HE; 2.76 eV), while keeping the

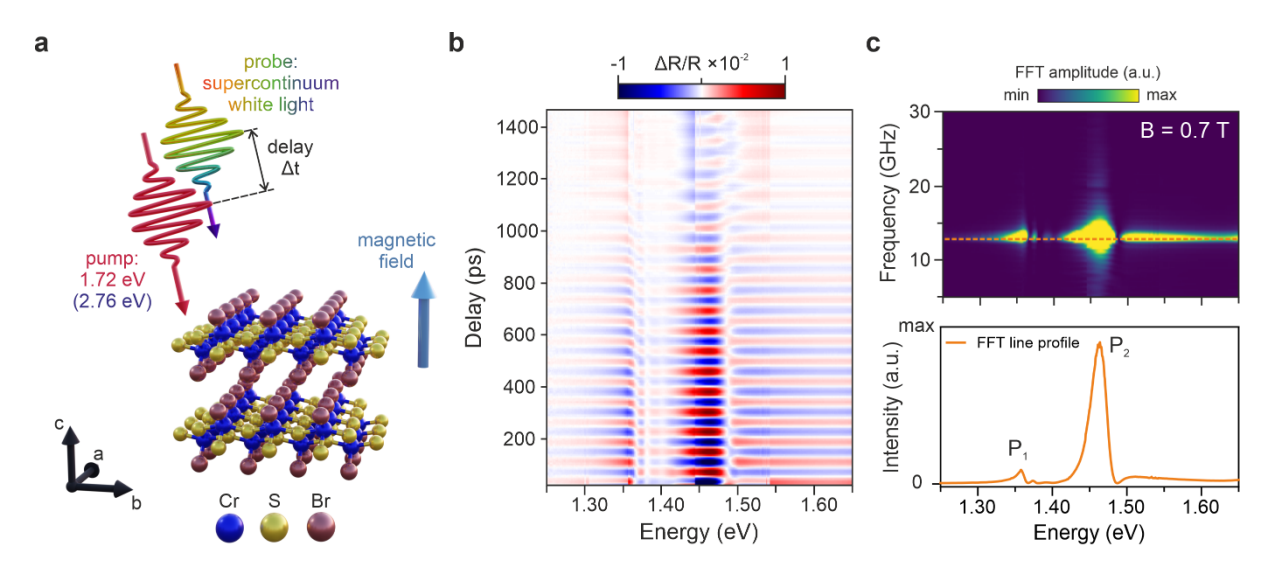


Figure 1: Experimental scheme and characterization of the transient reflectivity response of CrSBr for NR excitation at 1.72eV. a) Schematic illustration of the measurement geometry showing two stacked CrSBr layers, the applied magnetic field (B  $\parallel$  c), and the nearly normal-incidence pump and probe beams. b) Transient reflectivity signal ( $\Delta R/R$ ) at B = 0.7 T after subtraction of the incoherent background, showing clear oscillations across the probe energy range (1.25–1.65 eV). The oscillation amplitude is enhanced near 1.36 eV and 1.46 eV. c) Top: Two-dimensional fast Fourier transform (FFT) of the data in b), revealing a dominant mode at 12.74 GHz with intensity maxima around 1.36 and 1.46 eV, and a weaker but continuous response above 1.5 eV. Bottom: Line cut of the FFT amplitude at 12.74 GHz, highlighting the two distinct peaks P1 and P2 and their relative strengths.

incident fluence constant at 2.8 mJ/cm<sup>2</sup>. This allowed us to probe the system under markedly different excitation conditions, while the probe covered a supercontinuum range from 1.25 to 1.65 eV (see Methods for more details). We begin by discussing the NR excitation measurements, with the pump photon energy set to 1.72 eV. The pump and probe polarizations were aligned along the crystallographic a and b axes, respectively, maximizing sensitivity to anisotropic optical responses. The transient reflectivity dynamics were recorded under magnetic fields ranging from 0.2 T to 1.2 T.

**Figure 1b** and **c** present representative data at B = 0.7 T. After subtraction of the incoherent background (see Supplementary Information, SI), clear oscillations appear across the entire probe energy window, with enhanced amplitudes near 1.36 eV and 1.46 eV (**Figure 1b**). Fast Fourier transform (FFT) analysis reveals a single dominant frequency at 12.74 GHz, with negligible probenergy dispersion (**Figure 1c, top**). The FFT amplitude line cut at this frequency (**Figure 1c, bottom**) highlights two distinct peaks: a smaller peak (P1) at 1.36 eV and a broader, more intense peak (P2) near 1.46 eV, superimposed on a weak, nearly continuous background above 1.5 eV. Similar profiles were observed for all magnetic fields between 0.2 T and 1.1 T (see SI), with both peaks redshifting by approximately 7 meV (P1) and 9 meV (P2) as the field increases.

The magnetic-field dependence of this mode is summarized in **Figure 2a**. The oscillation frequency decreases systematically with increasing field and vanishes at B = 1.2T, identifying the mode as an inphase magnon, consistent with previous reports in the  $1.33-1.37\,\mathrm{eV}$  range<sup>30</sup>. However, unlike earlier studies that detected only localized exciton—magnon signatures, our measurements reveal pronounced oscillations throughout the  $1.25-1.65\,\mathrm{eV}$  probe window, demonstrating that the magnon couples more broadly to excitonic states than previously assumed.

In the SI we present transient reflectivity traces at B = 0.7 T for probe photon energies around the energy of P1. We identify a  $\pi$ -phase change occurring at 1.368 eV, as revealed by stepping the probe energy in 2 meV increments. Based on these observations, we assign P1 to the 1s Wannier exciton of CrSBr, in agreement with earlier reports<sup>27,29,33,34</sup>. The origin of P2 is less clear. Klein *et al.* reported distinct photoluminescence resonances above 1.45 eV<sup>35</sup>, while Linhart *et al.* attributed a feature at 1.45 eV in photoreflectance to transitions involving the second conduction band<sup>36</sup>. Most recently,

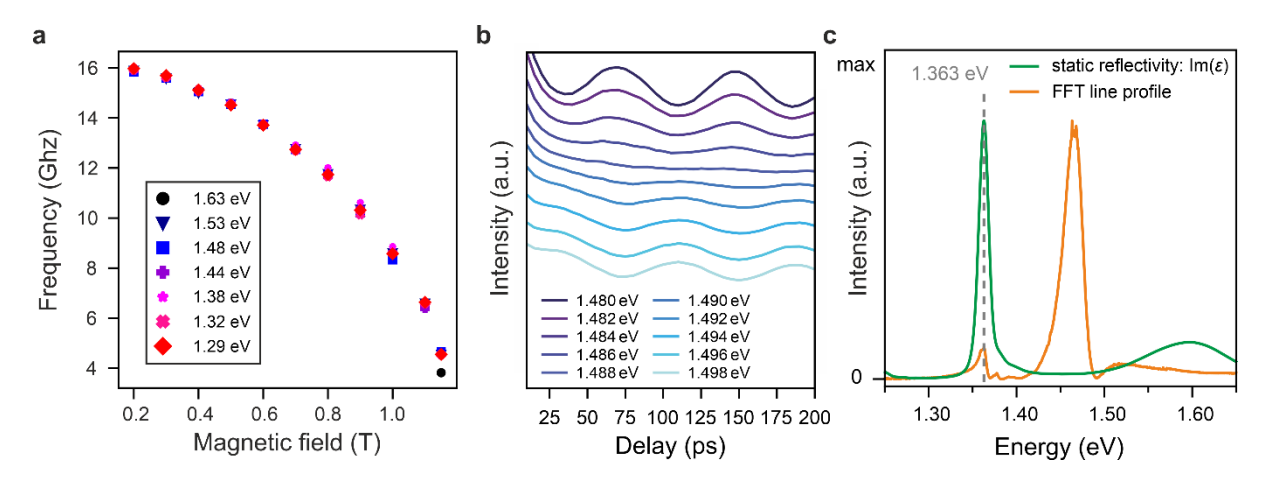


Figure 2: Magnetic-field evolution of the magnon mode,  $\pi$ -phase shift, and comparison between transient and static optical responses in CrSBr. a) Oscillation frequency extracted from the 2D FFT at NR excitation as a function of external magnetic field for several probe energies. The magnon frequency decreases with increasing field, while its dispersion with probe energy remains negligible. b) Phase of the transient reflectivity oscillations at the trailing edge of resonances P2 at B = 0.7 T. The traces are vertically offset for clarity. The oscillatory reflectivity exhibits a  $\pi$ -phase flip at the trailing edge of the resonance. c) Comparison of transient and static optical spectra at B = 0.2 T. Both curves are normalized to their respective maximum. The orange curve shows the FFT amplitude of the transient reflectivity, while the imaginary part of the dielectric function ( $\varepsilon_2$ , green) was obtained from the static reflectivity via Kramers–Kronig analysis. Both  $\varepsilon_2$  and the transient response exhibit a pronounced resonance at 1.363 eV, while no corresponding static feature appears near the second resonance observed only in the transient spectrum.

Sears *et al.* identified a dark exciton near 1.46 eV using resonant inelastic x-ray scattering<sup>32</sup>. To clarify these assignments, we examined the phase behavior of the transient signal around P2. Similar to the 1s exciton, the 1.46 eV feature exhibits a  $\pi$ -phase shift at its trailing edge, already suggesting its excitonic origin (**Figure 2b**).

The  $\pi$ -phase inversion provides a stringent criterion for identifying excitonic resonances. In transient reflectivity, the coherent magnon acts as a periodic perturbation of the complex dielectric function, and the resulting oscillatory component of  $\Delta R/R$  is proportional to the energy derivative of the reflectivity,  $\partial R/\partial E$ , evaluated at the probe photon energy. Across an excitonic resonance, the complex dielectric function  $\epsilon(E)$  exhibits a dispersive line shape that necessarily induces a zero-crossing in ∂R/∂E. As the probe energy moves through this point, the sign of the magnon-induced modulation reverses, producing a characteristic  $\pi$ -phase flip in the time-domain oscillations. This behavior is a hallmark of coherent modulation of a discrete optical transition and is not expected for continuum background absorption or for purely thermal responses. The observation of this  $\pi$ -phase shift at the trailing edge of P2 therefore demonstrates that the magnon couples to a well-defined optical resonance at 1.46 eV, providing compelling evidence that P2 corresponds to an excitonic transition rather than a continuum or defect-related feature. This behavior can be understood from the mechanism by which the magnon modulates the optical response. The coherent magnon oscillation periodically perturbs the dielectric function, and this modulation couples particularly strongly to excitonic resonances, which present sharp dispersive features in  $\varepsilon(E)$ . Bright excitons produce the familiar dispersive modulation in ΔR/R, while dark excitons—being optically silent in steady-state become visible only through their hybridization with the magnon-induced perturbation. In this way, the magnon effectively transfers the spectral signature of the dark exciton into the transient reflectivity response, enabling its indirect optical detection.

To further substantiate our assignment of P1 and P2, we measured static reflectivity spectra using a white light lamp polarized along the b axis. **Figure 2c** shows the imaginary part of the dielectric function  $\varepsilon_2$  (green), obtained from Kramers–Kronig analysis of the static reflectivity measured at B = 0.2 T. A sharp excitonic resonance appears at 1.363 eV, coinciding with the FFT peak P1 observed in the transient data (orange). Crucially, no corresponding feature in the static spectrum is visible at the

energetic position of P2 (1.46 eV). This discrepancy demonstrates that the 1.46 eV peak is invisible to conventional optical probes and emerges only through its interaction with the magnon signal in the transient reflectivity response. Based on these observations we assign P2 to the dark exciton recently reported in CrSBr<sup>32</sup>, emerging in the transient reflectivity signal through exciton-magnon coupling. Our results thus suggest that ultrafast probes can reveal hidden excitonic states otherwise inaccessible to steady-state optical probes.

All measurements so far were conducted using NR pump photon energy of 1.72 eV, above the ~1.5 eV band gap but near-resonance with the excitonic transitions in CrSBr. To probe the system under non-resonant conditions, we investigated the transient reflectivity response to HE excitations, using 2.76 eV pump photon energy, while keeping the incident fluence constant at 2.8mJ/cm² (see SI for details). Pumping in this HE regime generates hot carriers and transient heating, leading to a renormalization of magnetic exchange and anisotropy parameters<sup>37</sup>.

The less selective excitation further induces an inhomogeneous population of electronic states, which can modify the coherent magnon response. Figure 3a shows the magnon mode extracted from the FFT of the transient reflectivity for HE excitation at B = 0.7 T, to be compared to the NR excitation case shown in Figure 1c, where the magnon frequency remained essentially constant within 12.3–13.7 GHz (red lines) and showed no noticeable dispersion. Under HE excitation, however, the frequency exhibits a pronounced dependence on probe energy. This behavior precludes a simple horizontal amplitude cut to extract the amplitude profile of this mode as was done for the NR excitation case in Figure 1c (bottom). To circumvent this problem, we determined the maximum oscillation frequency for each probe energy prior to amplitude extraction and plot the corresponding amplitude profile in Figure 3b. A direct comparison between Figure 1c (bottom) and Figure 3b reveals marked differences between the two excitation regimes. First, the overall oscillation amplitude increases by roughly an order of magnitude (with respect to the background signal) for HE excitation. Second, peaks P1 and P2 shift in opposite directions: P1 appears at 1.353 eV for HE excitation, downshifted by ≈5 meV relative to the NR case, whereas P2 moves up to 1.478 eV, corresponding to an upshift of ≈15 meV. Third, the line shapes change qualitatively. At NR excitation, P1 exhibits an exponential leading edge, while at HE excitation it becomes nearly linear. Conversely, P2 steepens significantly at HE pumping. The interpeak region also differs: for HE excitation, no discernible intensity appears between the two main

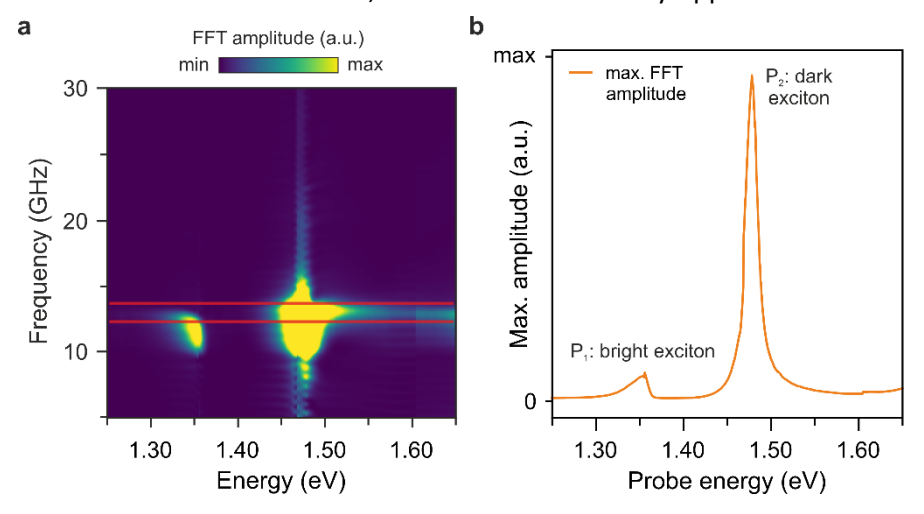


**Figure 3: Energy-dependent magnon response under HE excitation in CrSBr. a)** Two-dimensional FFT of the transient reflectivity at B = 0.7 T for HE excitation. The frequency distribution broadens substantially compared to NR and shows a pronounced deviation near the 1s exciton, indicating a strong energy-dependent modulation of the magnon mode. **b)** Amplitude profile of the magnetic mode extracted by tracking, for each probe energy, the frequency of maximum oscillation intensity rather than using a simple horizontal cut. The resulting amplitude spectrum displays two dominant peaks near 1.35 eV and 1.48 eV, shown in the insets, with significantly enhanced intensity and modified line shapes compared to resonant excitation.

peaks, in contrast to a weak intermediate feature at NR excitation. Likewise, beyond P2, the oscillation amplitude nearly vanishes for NR excitation before re-emerging, whereas in the HE case it merges smoothly into a continuum, consistent with an extended background response.

We now turn to the analysis of the phase behavior. Analogous to NR excitation, single-trace cuts at the falling edges of the peaks (see SI) show that the  $\pi$ -phase change becomes harder to identify for HE excitation due to the strong probe-energy dependence of the oscillation frequency. When restricting the time window to 0–50 ps, a phase reversal is nevertheless observed near 1.366 eV for P1, coinciding with the end of its trailing edge. Over the same interval, P2 exhibits similar but much more subtle behavior. We attribute the reduced phase contrast to the fact that, under high-energy excitation, the oscillation intensity does not fully decay to zero, thereby obscuring sharp phase inversions.

The frequency-domain linewidths also broaden significantly in the HE excitation regime. To quantify this effect, we extracted vertical cuts through the 2D FFT at the energies of maximum amplitude and plotted the corresponding frequency profiles in the SI. For NR excitation, P1 and P2 exhibit comparable full widths at half maximum (FWHM) of  $\approx 1.01\,\text{GHz}$ . Under HE excitation, the linewidths increase to  $\approx 2.26\,\text{GHz}$  (P1) and  $\approx 3.06\,\text{GHz}$  (P2), indicating enhanced dephasing in the HE regime. These linewidth changes are accompanied by a marked modification of the magnon's energy dispersion. Figure 4 compares the dependence of the magnon frequency on probe energy for NR and HE excitation. In the spectral region near the dark exciton P2 (1.5–1.65 eV; Figure 4a), the magnon frequency decreases by  $\approx 0.28\,\text{GHz}$  under HE excitation, whereas the decrease under NR excitation is negligibly small ( $\approx 0.08\,\text{GHz}$ ). Analogously, in the spectral region of the 1s exciton P1 the oscillation frequency decreases with increasing probe energy, as can be seen upon close inspection of Figure 3a. To highlight this trend more clearly, we selected two probe energies marking the onset of P1 (defined as the points where the signal reaches 10% of its maximum amplitude). As shown in Figure 4b, under HE excitation, the magnon frequency exhibits a pronounced, field-dependent reduction of 1.5–2.7 GHz (see inset of Figure 4b) within a narrow spectral window around 1.35 eV, in stark contrast to the

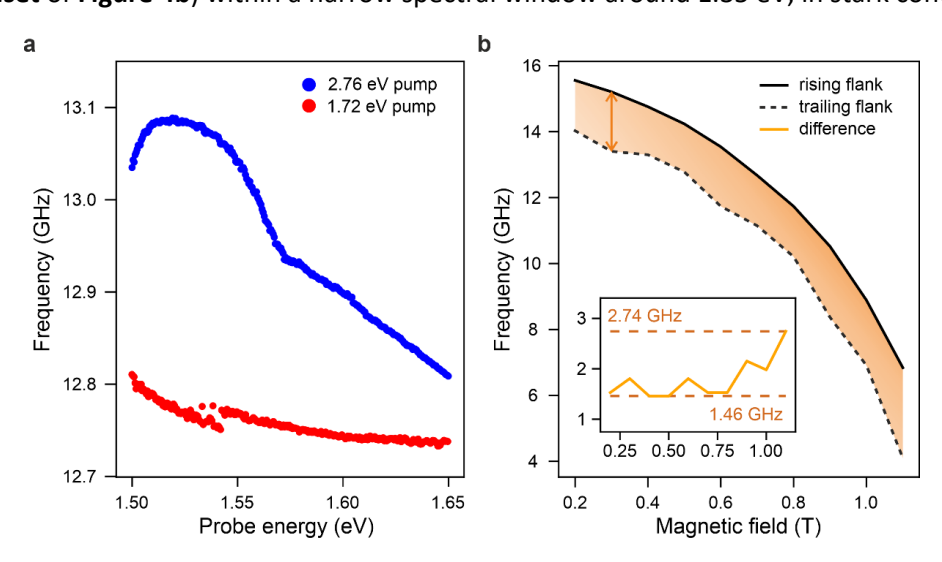


Figure 4: Energy and magnetic-field dependence of the magnon frequency in CrSBr under NR and HE excitation.
a) Dispersion of the magnon mode in the vicinity of P2 for B = 0.7 T. For NR excitation (1.72 eV), the magnon frequency exhibits an almost negligible dependence on probe energy above 1.5 eV, whereas for HE excitation (2.76 eV) there is a significant decrease of 0.28 GHz, indicating a strongly enhanced energy dispersion. b) Magnetic-field dependence of the magnon frequency near P1 under HE excitation. The magnon shows a pronounced downward bending within a narrow spectral window around 1.35 eV. To quantify this effect, the maximum oscillation frequency was extracted at the onset and end of P1 (defined at 10% of its peak amplitude). The black and grey curves correspond to these two positions, while the shaded region marks the full accessible frequency range across the resonance. The inset shows that the onset—end frequency separation reaches ≈1.5−2.7 GHz depending on the magnetic field, in stark contrast to NR excitation, where the variation remains below 0.5 GHz.

nearly dispersionless response observed for NR excitation. In summary, NR excitation yields a magnon mode that is almost dispersionless across both excitonic resonances, while HE excitation induces pronounced downward bending of the magnon frequency in the vicinity of P1 and P2. The enhanced linewidths and strong downward dispersion under HE excitation indicate that high-energy pumping transiently modifies the magnetic exchange and anisotropy landscape, thereby increasing the sensitivity of the magnon to excitonic resonances. The pronounced frequency softening near P1 and P2 is consistent with a scenario in which hot-carrier—induced renormalization enhances the exciton—magnon interaction and broadens the corresponding hybridized modes. Under these conditions, the magnon frequency becomes sensitive to the locally absorbed pump fluence, producing an inhomogeneous frequency profile that is correspondingly captured when the probe energy is tuned close to the excitonic resonances. In contrast, NR excitation preserves the intrinsic magnetic parameters, leading to a nearly dispersionless and weakly renormalized magnon response.

#### Conclusion

Our results demonstrate that magnetic order can fundamentally alter the optical selection rules of a van der Waals semiconductor by providing a coherent pathway to access otherwise hidden excitonic states. Using broadband femtosecond reflectivity on CrSBr, we uncover a dark exciton at 1.46 eV that is completely invisible in static spectra but becomes optically addressable through its coherent hybridization with a GHz magnon mode. This magnon-mediated visibility constitutes a general mechanism by which spin order enables optical readout of dark excitons and, more broadly, of excitonic degrees of freedom that lack radiative coupling.

We further show that the nature of this hybridization is tunable. High-photon-energy excitation strongly renormalizes the magnon dispersion and linewidths, enhancing the exciton—magnon interaction and selectively amplifying the dark-exciton response. These findings reveal that exciton—magnon coupling is not a fixed material property but a dynamically controllable channel through which magnetic correlations shape the excitonic landscape.

Taken together, our results position CrSBr as a model system in which magnetic order renders dark excitons both detectable and controllable. More generally, they establish ultrafast optical spectroscopy as a uniquely sensitive probe of hidden quasiparticles in magnetic van der Waals materials. By enabling the selective manipulation of hybrid spin—exciton modes, this work paves the way for engineered platforms for microwave-to-optical quantum transduction and other quantum technologies that rely on the interplay between electronic and magnetic excitations.

## Methods

## **Transient reflectivity setup**

Transient reflectivity measurements were carried out using an Yb-based femtosecond laser system (PHAROS, Light Conversion) operating at a central wavelength of 1040 nm and an average output power of 20 W<sup>38,39</sup>. The output beam was divided into pump and probe arms with powers of 13 W and 7 W, respectively. Pump and probe photon energies were tuned independently using optical parametric amplifiers (OPAs): the pump was set to either 1.72 eV or 2.76 eV, while the probe was tuned to 1.09 eV. A broadband supercontinuum probe was generated by attenuating the probe beam with a variable neutral-density filter and focusing it onto a 3-mm sapphire plate. After transmission through a short-pass filter (FESH1000, Thorlabs), the usable spectral window extended from 1.25 to 1.65 eV. The pump—probe delay was introduced by a motorized delay line (Newport) positioned in the pump path. Pump and probe beams were each routed through a half-wave plate and a polarizer, enabling independent control of polarization and power. Both beams were then focused onto the

sample surface using spherical mirrors. The reflected probe beam was collected, collimated, and spectrally dispersed by a diffraction grating, and subsequently detected on a calibrated multichannel diode array (Stresing), providing spectrally resolved transient-reflectivity signals with high sensitivity. The sample was mounted inside a cryostat capable of reaching temperatures down to 4 K. An external magnetic field of up to 2 T was applied out of plane using a superconducting solenoid integrated around the cryostat. Both pump and probe beams were directed onto the sample under (near-)normal incidence.

#### **Static reflectivity setup**

For the static reflectivity measurements, we used a broadband supercontinuum generated by a static white-light source (Thorlabs SLS201L/M). The beam polarization was controlled by a linear polarizer. All measurements were performed under normal incidence in the spectral range from 1.25 to 2.75 eV. A microscope objective (Mitutoyo  $50\times$  NIR) was used to focus the beam onto the sample, resulting in a spot size of approximately 10  $\mu$ m. The reflected light was first imaged onto a camera to determine and adjust the measurement position on the sample. By flipping a mirror out of the optical path, the reflected light was then directed to a compact spectrometer (Thorlabs CCS200/M). For data analysis, the measured spectra were normalized to the measured spectrum of the white-light source.

#### **Sample**

A custom-grown CrSBr crystal (HQ Graphene) with lateral dimensions of approximately  $8 \times 2$  mm (crystallographic a- and b-axis) was used for the measurements. Immediately prior to the experiments, the crystal surface was freshly cleaved using scotch tape, resulting in a final bulk thickness of about 2  $\mu$ m (crystallographic c-axis). Sample quality was assessed through Raman spectroscopy measurements (see Supplementary Information).

#### Al usage

After completion of the initial manuscript, the text was further refined regarding readability and clarity with the assistance of large language models. All suggested improvements were carefully reviewed by the authors and incorporated when deemed appropriate. No additional use of artificial intelligence was made during data acquisition, analysis, interpretation, or other aspects of this study.

## **Acknowledgments**

This work was supported by the Deutsche Forschungsgemeinschaft (DFG) through the Project dd2D (Project number 555818086.) and by the European Union's Horizon 2020 Research and Innovation Programme under Project SINFONIA, grant 964396. We gratefully acknowledge Cristian Manzoni (IFN-CNR) for his valuable support and advice during the setup and optimization of the transient reflectivity apparatus.

# **Bibliography**

- 1. Datta, B. *et al.* Magnon-mediated exciton–exciton interaction in a van der Waals antiferromagnet. *Nat. Mater.* **24**, 1027–1033 (2025).
- 2. Zhang, X.-X., You, Y., Zhao, S. Y. F. & Heinz, T. F. Experimental Evidence for Dark Excitons in

- Monolayer WSe<sub>2</sub>. Phys. Rev. Lett. 115, 257403 (2015).
- 3. Chand, S. B. *et al.* Interaction-driven transport of dark excitons in 2D semiconductors with phonon-mediated optical readout. *Nat. Commun.* **14**, 3712 (2023).
- 4. Bossini, D. *et al.* Ultrafast Amplification and Nonlinear Magnetoelastic Coupling of Coherent Magnon Modes in an Antiferromagnet. *Phys. Rev. Lett.* **127**, 77202 (2021).
- 5. Lachance-Quirion, D., Tabuchi, Y., Gloppe, A., Usami, K. & Nakamura, Y. Hybrid quantum systems based on magnonics. *Appl. Phys. Express* **12**, 070101 (2019).
- 6. Gibertini, M., Koperski, M., Morpurgo, A. F. & Novoselov, K. S. Magnetic 2D materials and heterostructures. *Nat. Nanotechnol.* **14**, 408–419 (2019).
- 7. Gong, C. *et al.* Discovery of intrinsic ferromagnetism in two-dimensional van der Waals crystals. *Nature* **546**, 265–269 (2017).
- 8. Huang, B. *et al.* Layer-dependent ferromagnetism in a van der Waals crystal down to the monolayer limit. *Nature* **546**, 270–273 (2017).
- 9. Gong, C. & Zhang, X. Two-dimensional magnetic crystals and emergent heterostructure devices. *Science* (80-. ). **363**, eaav4450 (2019).
- 10. Wang, G. *et al.* Colloquium: Excitons in atomically thin transition metal dichalcogenides. *Rev. Mod. Phys.* **90**, 21001 (2018).
- 11. Benini, M. *et al.* Light-driven modulation of proximity-enhanced functionalities in hybrid nano-scale systems. *Nat. Commun.* **16**, 7297 (2025).
- 12. Selig, M. *et al.* Excitonic linewidth and coherence lifetime in monolayer transition metal dichalcogenides. *Nat. Commun.* **7**, 13279 (2016).
- 13. Zhu, B., Chen, X. & Cui, X. Exciton binding energy of monolayer WS2. Sci. Rep. 5, 9218 (2015).
- 14. Xiao, J., Zhao, M., Wang, Y. & Zhang, X. Excitons in atomically thin 2D semiconductors and their applications. *Nanophotonics* **6**, 1309–1328 (2017).
- 15. Barré, E. *et al.* Optical absorption of interlayer excitons in transition-metal dichalcogenide heterostructures. *Science (80-. ).* **376**, 406–410 (2022).
- 16. Madéo, J. *et al.* Directly visualizing the momentum-forbidden dark excitons and their dynamics in atomically thin semiconductors. *Science* (80-. ). **370**, 1199–1204 (2020).
- 17. Schmitt, D. et al. Ultrafast nano-imaging of dark excitons. Nat. Photonics 19, 187–194 (2025).
- 18. Yang, K., Wang, G., Liu, L., Lu, D. & Wu, H. Triaxial magnetic anisotropy in the twodimensional ferromagnetic semiconductor CrSBr. *Phys. Rev. B* **104**, 144416 (2021).
- 19. Torres, K. *et al.* Probing Defects and Spin-Phonon Coupling in CrSBr via Resonant Raman Scattering. *Adv. Funct. Mater.* **33**, 2211366 (2023).
- 20. Klein, J. & Ross, F. M. Materials beyond monolayers: The magnetic quasi-1D semiconductor CrSBr. *J. Mater. Res.* **39**, 3045–3056 (2024).
- 21. Göser, O., Paul, W. & Kahle, H. G. Magnetic properties of CrSBr. *J. Magn. Magn. Mater.* **92**, 129–136 (1990).
- 22. Beck, J. Über Chalkogenidhalogenide des Chroms Synthese, Kristallstruktur und Magnetismus von Chromsulfidbromid, CrSBr. *ZAAC J. Inorg. Gen. Chem.* **585**, 157–167 (1990).
- 23. Scheie, A. *et al.* Spin Waves and Magnetic Exchange Hamiltonian in CrSBr. *Adv. Sci.* **9**, 2202467 (2022).
- 24. Liu, W. *et al.* A Three-Stage Magnetic Phase Transition Revealed in Ultrahigh-Quality van der Waals Bulk Magnet CrSBr. *ACS Nano* **16**, 15917–15926 (2022).
- 25. Telford, E. J. *et al.* Layered Antiferromagnetism Induces Large Negative Magnetoresistance in the van der Waals Semiconductor CrSBr. *Adv. Mater.* **32**, 2003240 (2020).
- 26. Wilson, N. P. *et al.* Interlayer electronic coupling on demand in a 2D magnetic semiconductor. *Nat. Mater.* **20**, 1657–1662 (2021).
- 27. Wang, T. *et al.* Magnetically-dressed CrSBr exciton-polaritons in ultrastrong coupling regime. *Nat. Commun.* **14**, 5966 (2023).
- 28. Marques-Moros, F., Boix-Constant, C., Mañas-Valero, S., Canet-Ferrer, J. & Coronado, E. Interplay between Optical Emission and Magnetism in the van der Waals Magnetic

- Semiconductor CrSBr in the Two-Dimensional Limit. ACS Nano 17, 13224–13231 (2023).
- 29. Meineke, C. *et al.* Ultrafast Exciton Dynamics in the Atomically Thin van der Waals Magnet CrSBr. *Nano Lett.* **24**, 4101–4107 (2024).
- 30. Bae, Y. J. *et al.* Exciton-coupled coherent magnons in a 2D semiconductor. *Nature* **609**, 282–286 (2022).
- 31. Sun, Y. *et al.* Dipolar spin wave packet transport in a van der Waals antiferromagnet. *Nat. Phys.* **20**, 794–800 (2024).
- 32. Sears, J. *et al.* Observation of Anisotropic Dispersive Dark-Exciton Dynamics in CrSBr. *Phys. Rev. Lett.* **135**, 146503 (2025).
- 33. Klein, J. *et al.* Sensing the Local Magnetic Environment through Optically Active Defects in a Layered Magnetic Semiconductor. *ACS Nano* **17**, 288–299 (2023).
- 34. Smolenski, S. *et al.* Large exciton binding energy in a bulk van der Waals magnet from quasi-1D electronic localization. *Nat. Commun.* **16**, 1134 (2025).
- 35. Klein, J. *et al.* The Bulk van der Waals Layered Magnet CrSBr is a Quasi-1D Material. *ACS Nano* **17**, 5316–5328 (2023).
- 36. Linhart, W. M. *et al.* Optical markers of magnetic phase transition in CrSBr. *J. Mater. Chem. C* **11**, 8423–8430 (2023).
- 37. Afanasiev, D. *et al.* Controlling the anisotropy of a van der Waals antiferromagnet with light. *Sci. Adv.* **7**, eabf3096 (2021).
- 38. Mertens, F. *et al.* Wide spectral range ultrafast pump-probe magneto-optical spectrometer at low temperature, high-magnetic and electric fields. *Rev. Sci. Instrum.* **91**, 113001 (2020).
- 39. Mertens, F. *et al.* Ultrafast Coherent THz Lattice Dynamics Coupled to Spins in the van der Waals Antiferromagnet FePS 3. *Adv. Mater.* **35**, 2208355 (2023).